

JGR Solid Earth

RESEARCH ARTICLE

10.1029/2021JB022084

Distribution of Rayleigh Wave Microseisms Constrained by Multiple Seismic Arrays

Ziying Wang^{1,2} , Fenglin Niu^{2,3} , Jianping Huang¹ , Zhenchun Li¹, and Haichao Chen³ 

Key Points:

- We investigate the distribution of Rayleigh wave microseisms by beamforming and Rayleigh wave amplitude-azimuth variation analyses
- Beam powers of seismic arrays at the two sides of the Pacific are back-projected to locate major sources of microseisms around the globe
- We identify a total of five primary microseism sources and two secondary microseism sources

Supporting Information:

Supporting Information may be found in the online version of this article.

Correspondence to:

J. Huang,
jphuang@upc.edu.cn

Citation:

Wang, Z., Niu, F., Huang, J., Li, Z., & Chen, H. (2021). Distribution of Rayleigh wave microseisms constrained by multiple seismic arrays. *Journal of Geophysical Research: Solid Earth*, 126, e2021JB022084. <https://doi.org/10.1029/2021JB022084>

Received 16 MAR 2021

Accepted 30 JUL 2021

¹Department of Geophysics, China University of Petroleum (East China), Qingdao, China, ²Department of Earth, Environmental, and Planetary Sciences, Rice University, Houston, TX, USA, ³State Key Laboratory of Petroleum Resources and Prospecting, Unconventional Petroleum Research Institute, China University of Petroleum at Beijing, Beijing, China

Abstract Microseisms are the most energetic signals of Earth's ambient noise field. Locating the sources of microseisms helps us to understand arrivals on noise cross-correlation functions (NCFs) and the asymmetric amplitude of Rayleigh waves on the positive and negative parts of the NCFs. Using a dense broadband seismic array in eastern China, we investigated temporal and spatial characteristics of Rayleigh wave microseisms in the frequency range of 45–155 mHz by conducting beamforming and Rayleigh wave amplitude-azimuth variation analyses. Seasonal variations of incident direction are clearly observable at the primary microseisms frequency band (45–95 mHz) but are less prominent at the secondary microseisms frequency band (95–155 mHz). The beamforming and amplitude-azimuth variation analyses also indicated that microseisms arriving at the array are dominantly from five back azimuthal bands. To locate the source areas of the observed microseisms, we combined noise data from two additional arrays in southern California and employed a multi-array beamforming technique to constrain plausible microseisms' source areas. We found that microseisms of the five azimuthal bands were excited at the Southern Ocean, western coast of Europe, coastal areas of the North Pacific Ocean, the Kerguelen Islands in the southern Indian Ocean, and the Polynesia islands in the South Pacific Ocean, respectively.

Plain Language Summary Ambient noise is continuous and low-amplitude seismic waves, widely recorded on the Earth. The microseism is a part of the ambient seismic wave field with the period from 2 to 50 s, primarily generated by the interaction between the ocean waves and the Earth. In this study, we analyze the temporal and spatial characteristics of Rayleigh wave microseisms recorded in eastern China. Although some studies investigated the characteristics of microseisms, origins of microseisms related to Rayleigh waves recorded in this region are yet to be studied. We use the beamforming method to give plausible microseism source areas. Rayleigh wave amplitude-azimuth variation analysis is used in a complementary way to qualitatively verify the beamforming results. To constrain the source areas, we combine another two arrays in southern California. According to the results of multi-array combined method, we identify microseism sources and use other types of data (Rayleigh wave amplitude, ocean wave height, and ice distribution) to verify and interpret the sources.

1. Introduction

Ambient noises are ubiquitous low-amplitude signals generated by couplings between the atmosphere, ocean, and solid earth (Nishida, 2017). The characteristics and excitation mechanism of ambient noise have been studied for decades (Hasselmann, 1963; Longuet-Higgins, 1950). As the development of seismic interferometry, seismic records of ambient noise are turned to signals by cross correlation, which is the basis for ambient noise tomography to study crustal and uppermost mantle structure (e.g., Moschetti et al., 2007; Shapiro et al., 2005; Yang et al., 2007, 2010).

Microseisms are the most energetic signals of Earth's background noise field with a frequency range of 20–500 mHz (2–50 s in period) (Nishida, 2017; Wang et al., 2018). The excitation of microseisms is due to the interaction between ocean waves and the solid earth, which is affected by bathymetry and the occurrence of strong storms (Kedar et al., 2008; Longuet-Higgins, 1950; Retailleau et al., 2017). Therefore, microseisms can be continuous or transient, local or distant signals depending upon their source areas. Since irregular

storm happens and global ocean activity has seasonal variations, the distribution of microseisms changes over time.

Microseisms are categorized into two types: (a) primary, or single-frequency microseisms (PM) between 20 and 100 mHz and (b) secondary, or double-frequency microseisms (SM) between 100 and 500 mHz (Ardhuin et al., 2011; Longuet-Higgins, 1950). The dominant frequency of PM is about 70 mHz which is the same as the typical frequency of ocean swell (Nishida, 2017). PM are generated by the impact of ocean waves against shallow seafloor (Hasselmann, 1963). The dominant frequency of SM is about 150 mHz, roughly twice the typical frequency of ocean swell (Nishida, 2017). The excitation of SM needs nonlinear interactions between ocean waves with similar period propagating in opposite directions (Ardhuin et al., 2011; Bromirski et al., 2005; Longuet-Higgins, 1950). The energy of SM is much higher than those of PM (Ying et al., 2014).

Much work has been done to study sources of microseisms using seismic data. Beamforming has been applied to continuous data to estimate the incident direction and apparent propagation speed (or slowness) of microseisms and other seismic signals (Gerstoft et al., 2006; Gerstoft & Tanimoto, 2007; Traer et al., 2012; Xiao, Xue, Pan, & Gao, 2018). Based on the measured slowness, one can determine whether a signal is a surface wave or body wave arrival. For a body wave arrival, since the measured slowness can be used to determine the epicentral distance of the source, it is possible to back-project the recorded energy to a specific source area, which is known as the back-projection method (Gerstoft et al., 2008; Liu et al., 2016; Nishida & Takagi, 2016; Wang et al., 2018; Zhang et al., 2010). The method was developed for teleseismic imaging of large earthquake ruptures (Ishii et al., 2007; Xu et al., 2009). SM sources exciting energetic body waves can be located with high resolution using the back-projection method.

The beamforming-back-projection method is, however, inapplicable for locating microseism sources of ballistic surface wave arrivals, as the measured slowness/apparent velocity cannot be used to constrain epicentral distance. In principle, anywhere along the great circle path extending from the array center in the incident direction could be a potential source region of the ambient noise recorded by the array. Other types of data, such as ocean wave height, have been used to infer potential source regions along the great circle paths (Traer et al., 2012; Xiao, Xue, Yang, et al., 2018). On the other hand, off great-circle sources usually appear on noise cross-correlation functions (NCFs) as precursory arrivals (Retailleau et al., 2017; Zeng & Ni, 2010, 2014) and can be located through grid searching. Zeng and Ni (2010) tracked the source of an anomalous arrival observed at NCFs computed from stations across the Japan Sea to magma motions underneath a volcano in southwest Japan. Retailleau et al. (2017) observed a precursory arrival on NCFs between cross-Atlantic stations and employed a grid search method to attribute it to a source near Iceland.

In addition to beamforming analysis, directional variations of Rayleigh wave amplitude on NCFs have been used to infer the azimuthal distribution of noise sources (Stehly et al., 2006; Tian & Ritzwoller, 2015; Yang & Ritzwoller, 2008). However, this method requires a significant amount of time stacking to obtain high-quality NCFs, and station pair directions are generally unevenly distributed, therefore it has a lower temporal and directional resolution as compared to the beamforming analysis, which is the main technique in estimating noise direction. Nishida (2017) provides a good summary of the complementary nature of the two methods. On the other hand, beamforming usually employs a uniform velocity model in computing time offsets between the array center and individual stations, therefore velocity heterogeneities underneath the array could affect the correct determination of back azimuth (Nishida, 2017). This problem could be severe when a large aperture array is used, and data frequency is high. Several techniques (Gal et al., 2018; Juretzek & Hadziioannou, 2017) have been proposed to incorporate lateral heterogeneities in the beamforming analysis to better estimate source directions.

Most previous studies located PM sources at shallow coastal areas. Observed microseismic energy comes from near-shore regions of the North Atlantic, and North and South Pacific with obvious seasonal variation (Cessaro, 1994; Juretzek & Hadziioannou, 2016; Retailleau et al., 2017; Tian & Ritzwoller, 2015; Traer et al., 2012). This is consistent with the theory of PM generation due to ocean storms coupling with solid earth. At SM frequency band, wave-wave interactions generate strong body waves and relatively weak surface waves at coastal areas and open sea, including the North Pacific, North Atlantic, South Pacific, and the southern Indian Ocean (Landès et al., 2010; Liu et al., 2016; Pyle et al., 2015; Tian & Ritzwoller, 2015; Traer

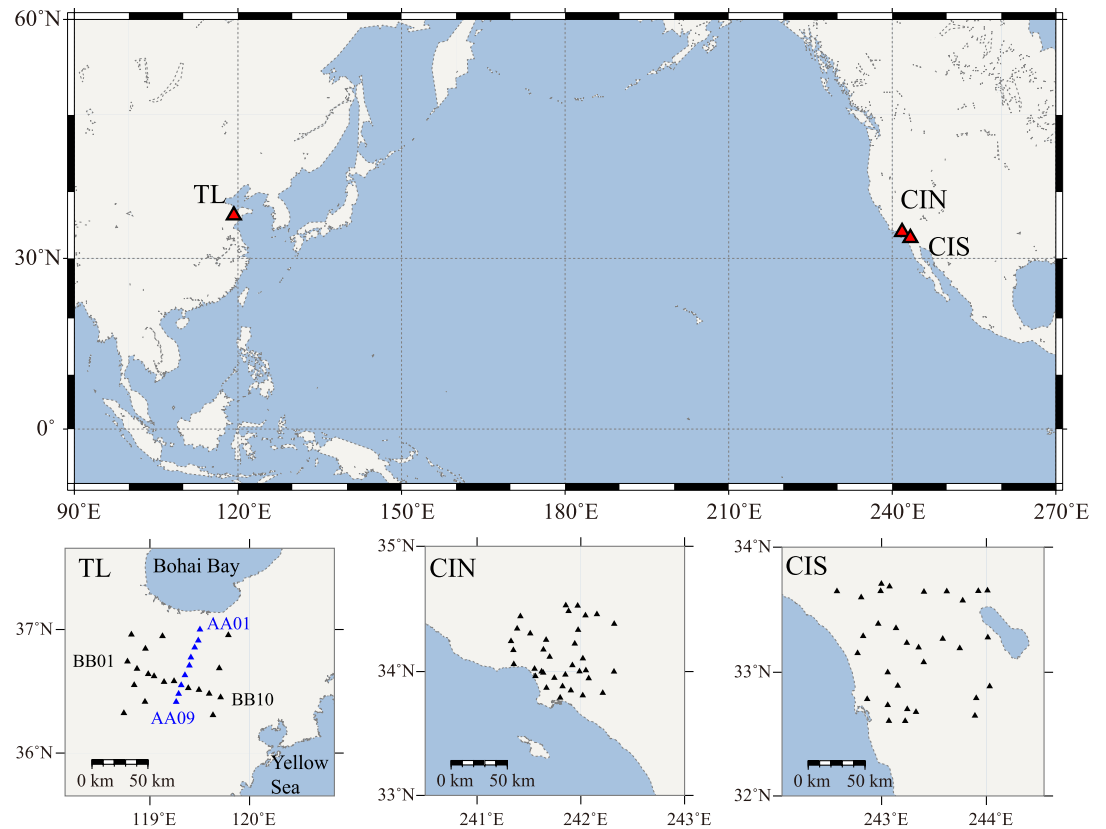


Figure 1. Locations of the arrays used in this study are shown in the upper panel. We use three arrays, TL array (28 stations) in eastern China, CIN array (35 stations) and CIS array (31 stations) in southern California. The CIN and CIS arrays are formed by stations of the Southern California Seismic Network with an aperture and interstation distance similar to the TL array. The center of each array is marked by a red triangle and labeled with the array name. Individual array configurations are shown in the bottom row. The black triangles indicate the locations of seismic stations. Station AA01–AA09 are colored in blue to distinguish between AA line and BB line. The TL array is surrounded by the Bohai Bay to the northeast and the Yellow Sea to the southeast.

et al., 2012; Wang et al., 2018; Ward Neale et al., 2018). Transient strong storms like typhoons or hurricanes were tracked by locating body wave sources (Gerstoft et al., 2008; Liu et al., 2020; Park & Hong, 2020; Retailleau & Gualtieri, 2019; Zhang et al., 2010). However, it is still unclear if the PM and SM share shallow water areas as exciting locations (Bromirski & Duennebie, 2002; Cessaro, 1994).

In this study, we first investigated temporal and spatial characteristics of Rayleigh wave PM and SM using a dense broadband seismic array deployed across the northern segment of the Tanlu fault in eastern China (hereafter referred to as the TL array). Although SM sources generating body waves have been investigated with the ChinArray (Liu et al., 2016; Wang et al., 2018), origins of microseisms related to Rayleigh waves recorded in this region are yet to be studied. Here, we conducted beamforming and Rayleigh wave amplitude-azimuth variation analyses to investigate the seasonal variations and azimuthal distribution of microseisms. Next, we back-projected the beam power along great circle paths to search for potential source regions. By combining the TL array and two closely located arrays with a similar configuration in southern California, we constrained plausible source areas using the multi-array back-projection technique. Finally, based on the multi-array combined images, we inferred PM and SM source locations at a global scale.

2. Data and Methods

In this study, we first use data from 28 broadband stations of the TL array deployed across the Weifang segment of the Tanlu fault in eastern China (Figure 1). Three-component continuous seismic data were recorded for 10 months from September 2017 to June 2018. In addition, we downloaded vertical continuous

records of the Southern California Seismic Network (CI) of the same period from the Southern California Earthquake Data Center (SCEDC, 2013). Based on the data from the TL array and two arrays in southern California, we employed a multi-array back-projection method to constrain source locations of Rayleigh wave microseisms.

2.1. Beamforming

We first use the beamforming method to obtain the directionality of surface wave microseisms. Continuous vertical-component data are cut into one-day time series, resampled at 1 Hz, and filtered from 10 to 400 mHz. Then the data are split into non-overlapping 512-s long segments. We compute the standard deviation σ of each segment and truncate signal amplitude with a clipping threshold of σ , that is, all data points with absolute values greater than σ are set to $\pm\sigma$. Then we normalize the seismic data in the frequency domain to reduce narrow band signals that could be a non-microseismic transient (Gerstoft & Tanimoto, 2007; Traer et al., 2012). The center of the array is calculated by averaging the latitude and longitude of all stations. Next, we apply beamforming analysis in the frequency domain under the assumption that waves recorded by the array can be represented by a superposition of plane waves (Gerstoft & Tanimoto, 2007). The vertical-component array data are Fourier transformed to a complex-valued vector \mathbf{v} containing the response of all stations in the array. In the frequency domain, the beam power value $b(\omega, t, s_x, s_y)$ for a given frequency ω and slowness (s_x, s_y) is expressed as,

$$b(\omega, t, s_x, s_y) = \mathbf{p}(\omega, s_x, s_y)^\dagger \mathbf{C}(\omega, t) \mathbf{p}(\omega, s_x, s_y), \quad (1)$$

where \dagger denotes the transpose conjugate. $\mathbf{C}(\omega, t)$ is the cross-spectral density matrix,

$$\mathbf{C}(\omega, t) = \frac{1}{K} \sum_{k=1}^K \mathbf{v} \mathbf{v}^\dagger. \quad (2)$$

Here k is the segment index, and K is the total number of segments. We set $K = 10$ in this study, indicating temporal averaging over 10 segments, which is approximately one and a half hours (512×10 s). $\mathbf{p}(\omega, s_x, s_y)$ is the plane-wave response of the seismic array in the frequency domain, given by

$$\mathbf{p}(\omega, s_x, s_y) = e^{i\omega \mathbf{s} \mathbf{r}}, \quad (3)$$

where \mathbf{s} is the assumed plane wave slowness vector (s_x, s_y) . \mathbf{r} is the location vector of a station measured from the array center.

All beamforming results at a certain frequency band are summed up monthly in order to identify Rayleigh wave incident directions and to investigate seasonal variations of the noise distribution. We vary s_x and s_y in the range of -0.5 to 0.5 s/km with an increment of 0.002 s/km. The observed beam power spectrum \mathbf{B}_0 is a 501×501 gridded image. An example of the beam power spectrum at the frequency band of 55–65 mHz using the TL array data recorded in June 2018 is shown in Figure 2a. In this case, the beamforming image is of low resolution since the array response function (ARF) has a blurring effect. Removing ARF can improve the resolution of the observed 2-D spectrum (Nishida et al., 2008). The ARF of the plane wave at frequency ω and slowness (s_x, s_y) can be written as (Rost & Thomas, 2002):

$$a(\omega, s_x, s_y) = \left| \frac{1}{N} \sum_{n=1}^N e^{i\omega \mathbf{s} \mathbf{r}_n} \right|^2. \quad (4)$$

Here N is the number of stations in the array. Like beam power spectrum, the ARF spectrum is also a 501×501 gridded image, denoted as \mathbf{A} . Next, we deconvolve ARF (Figure 2b) from the observed beam power spectrum \mathbf{B}_0 by the accelerated Richardson-Lucy deconvolution algorithm (Biggs & Andrews, 1997; Richardson, 1972), which is expressed as

$$\mathbf{B}'_{m+1} = \mathbf{B}_m \cdot \left(\mathbf{A} \otimes \frac{\mathbf{B}_0}{\mathbf{A} * \mathbf{B}_m} \right), \quad (5)$$

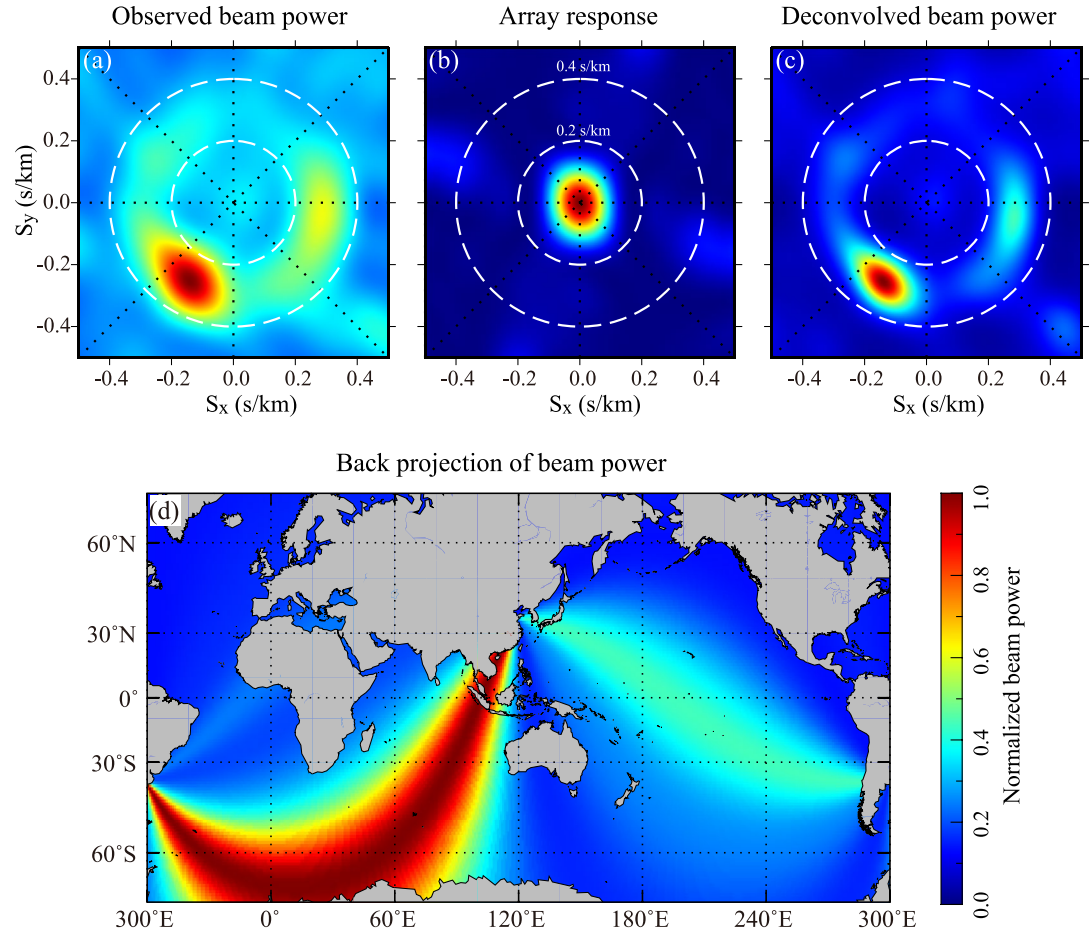


Figure 2. An example of the Richardson-Lucy deconvolution and back-projection applied to the observed beam power at the frequency band of 55–65 mHz using the TL array data recorded in June of 2018. (a) Observed beam power spectrum. (b) Array response function of the TL Array. (c) Deconvolved beamformer output after 10 iterations. Surface wave slowness window is indicated by white dashed circles (0.2–0.4 s/km). (d) The back-projection of deconvolved beamforming output to the global $1^\circ \times 1^\circ$ grid set based on their corresponding back azimuth. All images are normalized by the maximum energy.

$$\mathbf{B}_{m+1} = \begin{cases} \mathbf{B}'_{m+1}, & m = 0, \\ \mathbf{B}'_{m+1} + \lambda_m [\mathbf{B}'_{m+1} - \mathbf{B}'_m], & m \geq 1, \end{cases} \quad (6)$$

where \mathbf{B}_0 is the observed beam power spectrum, which is also the initial input of iterative deconvolution operation. Equation 5 shows the iterative procedure of the conventional Richardson-Lucy algorithm, where \mathbf{B}'_{m+1} is a deconvolved spectrum of the current iteration. Here we employ an accelerated Richardson-Lucy deconvolution algorithm (Equation 6). From the second iteration, a correction term is added to \mathbf{B}'_{m+1} , which is calculated by the difference between the current iteration and the previous iteration. Then we have the deconvolved spectrum \mathbf{B}_m based on the accelerated algorithm. λ_m is the acceleration factor, defined as $\lambda_m = \frac{\sum \mathbf{g}_m \otimes \mathbf{g}_m}{\sum \mathbf{g}_m \otimes \mathbf{g}_m}$, where Σ sums all elements in the matrix. The gradient \mathbf{g}_m at m -th iteration is defined as $\mathbf{g}_m = \mathbf{B}'_{m+1} - \mathbf{B}'_m$. The value of λ_m is limited between 0 and 1. \otimes is the correlation operator. $*$ is the convolution operator. \cdot and $/$ denote element-wise production and division, respectively. In general, the deconvolved beamforming spectra become stable after a few iterations, so we keep the iteration number of 10. The deconvolved beamforming output is further normalized by its maximum, shown in Figure 2c.

2.2. Azimuthal Variations of Rayleigh Wave Amplitudes

We verify the back-azimuth range of sources determined from beamforming through analyzing the directional dependence of Rayleigh wave amplitudes calculated from NCFs. We use the vertical component recorded by the TL array to compute vertical-vertical NCFs. The preprocessing procedure applied here is similar to that described by Bensen et al. (2007). We summarize preprocessing steps as follow: (a) cutting seismic data into one-day segments, resampling the continuous data at 10 Hz, removing mean and trend, (b) band-passing from 10 to 500 mHz, (c) temporal normalization and spectral whitening, and (d) performing cross correlation. The temporal normalization method we used is running-absolute-mean normalization proposed by Bensen et al. (2007).

We calculate daily NCFs between all station pairs of the TL array. After that, the daily NCFs are stacked monthly. Figure 3 shows examples of one-month-stacked NCFs in the frequency range of 45–155 mHz along the AA and BB lines. At the top, we plot eight NCFs between AA09 and the other eight stations along the AA line (AA01-AA08) using 1-month data of June (Figure 3a) and December (Figure 3b). Rayleigh wave arrivals are highlighted in shaded time windows. The positive lags of NCFs correspond to north-northeastward waves propagating from the virtual source station AA09 to these receiver stations, while the negative segments pick up waves propagating in the opposite direction, that is, the SSW direction. The amplitude of Rayleigh waves on the positive sides (yellow shaded) is much larger than those on negative sides (gray shaded), indicating that microseism sources are largely distributed in the south. Such an asymmetric relationship in Rayleigh wave amplitude is observed in NCFs derived from both summer and winter records and is also consistent with the prominent arrival from the SSW direction shown in the beamforming example of Figure 2c.

The NCFs computed along the BB line using BB10 as the virtual source are shown in the bottom part of Figure 3. Both the summer (Figure 3c) and winter month NCFs (Figure 3d) show dominant Rayleigh wave arrivals on the positive sides, suggesting a potential noise source located in the ESE direction to the array. This is also consistent with the ESE arrival shown in the beamforming example of Figure 2c. Compared to the AA-line NCFs, the BB-line NCFs show high-amplitude precursory arrivals near the zero lag, which suggests there is a coherent noise source located in the direction perpendicular to the BB line.

Because absolute amplitude information is lost during the processing of ambient noise data, here we use signal-to-noise ratios (SNRs) to measure relative Rayleigh wave amplitudes. SNRs are estimated by calculating the ratios between the maximum absolute amplitudes of the Rayleigh waves in signal windows and the root-mean-squared amplitudes of NCFs in the coda windows. Signal windows are determined by dividing the distances between station pairs by surface wave velocity (2.5~3.5 km/s), while noise windows are defined as 100-s long segments of NCFs starting from 200 s after the ends of signal windows.

Since SNR measurements are influenced by the numbers of daily NCFs used in the stacking and interstation distance, it is necessary to correct SNR before investigating the relationship between SNR and pair direction. First, we correct SNR for interstation distance using the equation,

$$SNR_{cd} = SNR \cdot \sqrt{\frac{D}{50}}, \quad (7)$$

where SNR is the raw SNR of a stacked NCF calculated from a pair of stations with a distance of D km. SNR_{cd} is the SNR after correcting interstation distance to 50 km.

In addition to the above distance correction, we further make another correction on the number of daily NCFs used in stacking, as we expect that SNR is proportional to the square root of stacked times (Tian & Ritzwoller, 2015). We employ a stack number of 30 days to normalize the distance corrected SNR:

$$SNR_{cs} = SNR_{cd} \cdot \sqrt{\frac{30}{N_{stacked}}}, \quad (8)$$

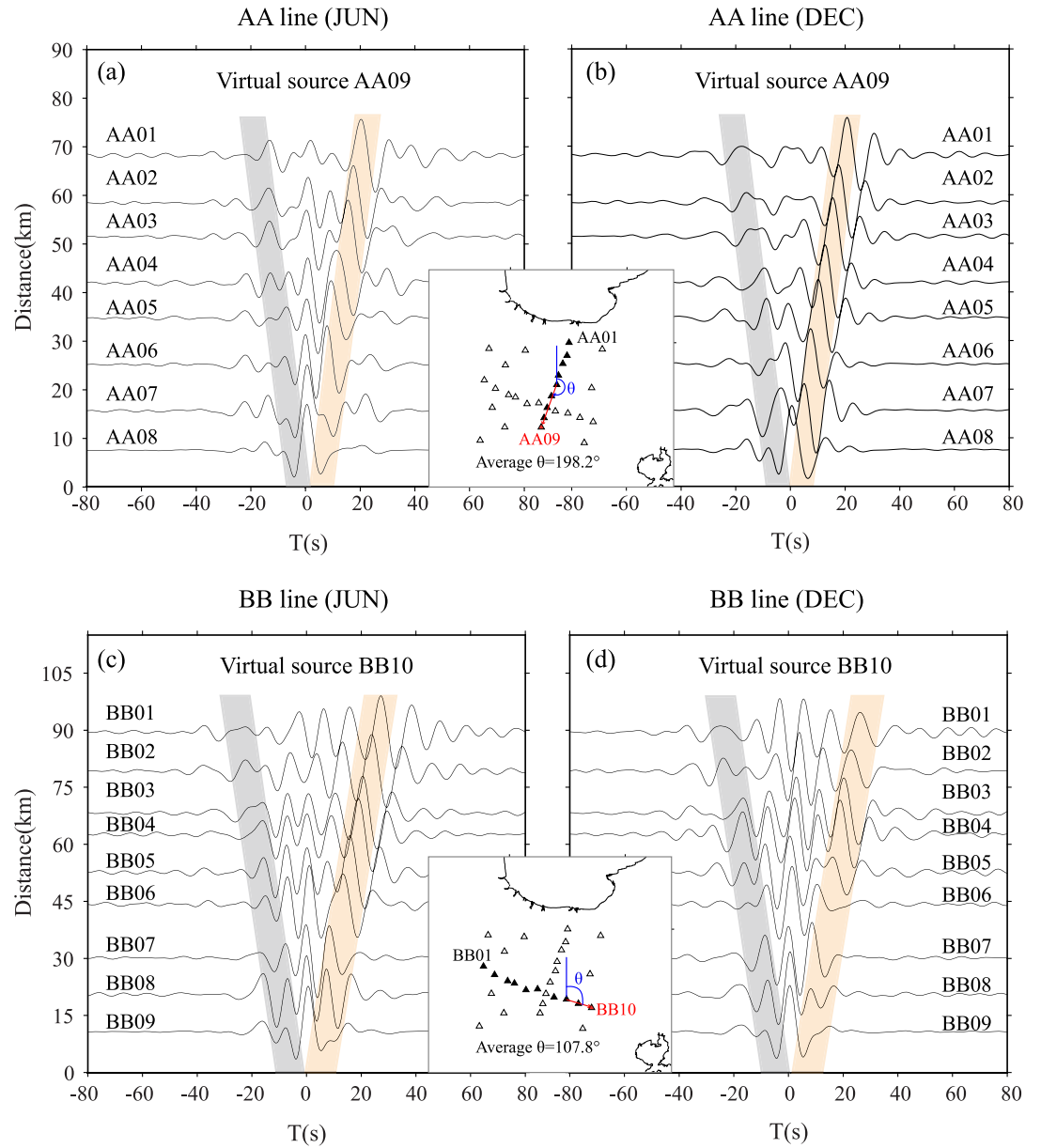


Figure 3. Examples of 1-month-stacked NCFs in the frequency range of 45–155 mHz along the AA and BB lines of TL array. In the top row, we plot 8 NCFs between AA09 and other eight stations along the AA line (AA01–AA08) using 1 month data of June 2018 (a) and December 2017 (b). In the bottom row, 9 NCFs are between BB10 and other nine stations along the BB line (BB01–BB09). Rayleigh wave arrivals are highlighted in shaded time windows. We indicate the stronger signal window by coloring it yellow. The two figures inserted in the middle illustrate the station locations and the definition of back azimuth θ . Correlated stations are marked by black-filled triangles. Other stations are marked by open triangles. The blue line points to the geographic north. The red line extends along the direction of AA line and BB line. The averaged back azimuth is 198.2° for the NCFs along AA line, and is 107.8° for the NCFs along BB line.

where SNR_{cs} is the SNR after correcting stacked times, and $N_{stacked}$ is the number of stack days. Finally, we sort the SNR_{cs} as a function of the azimuth of the great circle ray path between the virtual source and station, which is defined clockwise from north. We average the SNRs in 30° azimuthal bins to obtain the azimuthal variation of SNR. The uncertainty is calculated by dividing the standard deviation of SNRs with the squared root of the pair number in each azimuthal bin.

2.3. Locating Noise Sources Using Multi-Array Back-Projection

To locate potential sources along the great circle path, we introduce a multi-array back-projection method. To do so, we first conduct the beamforming analysis described in Section 2.1 for each array. Next, we discretize the earth's surface with a set of $1^\circ \times 1^\circ$ grids. For each grid, we compute the back azimuths from the grid to each array center. Finally, we back-project the beamforming results of each array to the global $1^\circ \times 1^\circ$ grid set based on their corresponding back azimuth. We assume a surface wave slowness window of 0.2–0.4 s/km and back-project the beam power maximum in this window along certain back azimuth to all the appropriate grid points with the right back azimuth:

$$BP_i(lon, lat)(\varphi) = \max[B_i(\omega, s, \varphi)], \quad 0.2 \text{ s/km} < s < 0.4 \text{ s/km}. \quad (9)$$

Here $BP_i(lon, lat)(\varphi)$ is the back-project of beamforming result of the i th array at the grid point (lon, lat) that has a back azimuth of φ . $B_i(\omega, s, \varphi)$ is the beam power of i th array at slowness $s = \sqrt{s_x^2 + s_y^2}$ and back azimuth $\varphi = 90 - \arctan(s_y/s_x)$. An example $BP(lon, lat)(\varphi)$ is shown in Figure 2d, which is the back-projection of the beam power shown in Figure 2c. Since both the PM and SM are originated from ocean waves, we block the value on the continents by coloring the land gray. When multiple arrays are available, the total beam power is defined as the product of individual beam power of all the N arrays:

$$BP_{total}(lon, lat)(\varphi) = \prod_{i=1}^N BP_i(lon, lat)(\varphi). \quad (10)$$

We select stations from the CI Network to form two more arrays with an aperture and interstation distance similar to the TL array. Station locations of the two selected arrays are shown in Figure 1. The two arrays are referred to as the North CI Array (CIN) and South CI Array (CIS), respectively. As the two CI arrays are very close to each other, we first back-projected the beamforming results of the two arrays to obtain the combined beam power at all the grid points. The combination is very effective in removing the contributions of local sources. On the other hand, microseisms generated at distant regions are expected to remain as high beam power on the combined image since their great circle paths to the closely located arrays are nearly parallel to each other. We further normalize the back-projected beam power of the TL array and two CI arrays by their maximum amplitudes, respectively. This is to ensure that the beam power from the two locations has the same contribution to the final result. Finally, we compute the element-wise production of the two back-projection images of the TL and CI array to produce the final back-projection image.

3. Results

3.1. Seasonal Variations

We apply beamforming analysis to the TL array data at the frequency bands of PM (45–95 mHz) and SM (95–155 mHz). To investigate the seasonal variations of microseisms, we first stack beamforming results from 5,120-s long non-overlapping segments to generate seasonal beamforming spectra: autumn (September 2017 to November 2017), winter (December 2017 to February 2018), spring (March 2018 to May 2018), and summer (June 2018). Since we only have 10-months of recording, so the summer beamforming spectrum is the result of 1-month stack. The seasonal beamforming spectra of the PM and SM are shown in the left and right columns of Figure 4, respectively. The beamforming images indicate a highly heterogeneous distribution and seasonal variations in the arrival direction of microseisms (Figure 4).

In the PM frequency band, the TL array beamforming images (Figures 4a–4d) are dominated by arrivals with a slowness between 0.25 s/km and 0.4 s/km, that is, 2.5–4.0 km/s in apparent velocity, suggesting that they are most likely surface waves. Roughly, these surface wave arrivals come from three azimuthal bands: $\sim 45^\circ - 145^\circ$, $\sim 180^\circ - 225^\circ$, and $\sim 290^\circ - 350^\circ$ (Figures 4a–4d). The strength and central azimuth of these arrivals appear to change with seasons. In the spring (Figure 4c) and summer (Figure 4d), the strongest arrival is seen from $\sim 110^\circ$ (\sim ESE, M2) and the second strongest arrival is from $\sim 210^\circ$ (SSW, M1). A third weak signal can be found from the NW direction mainly in spring (Figure 4c). In autumn (Figure 4a) and winter (Figure 4b), the SSW arrival becomes the strongest signal in the beamforming images, and its direction also shifts slightly to the south with an azimuth of $\sim 190^\circ$. The ESE signal becomes much weaker and is diffused

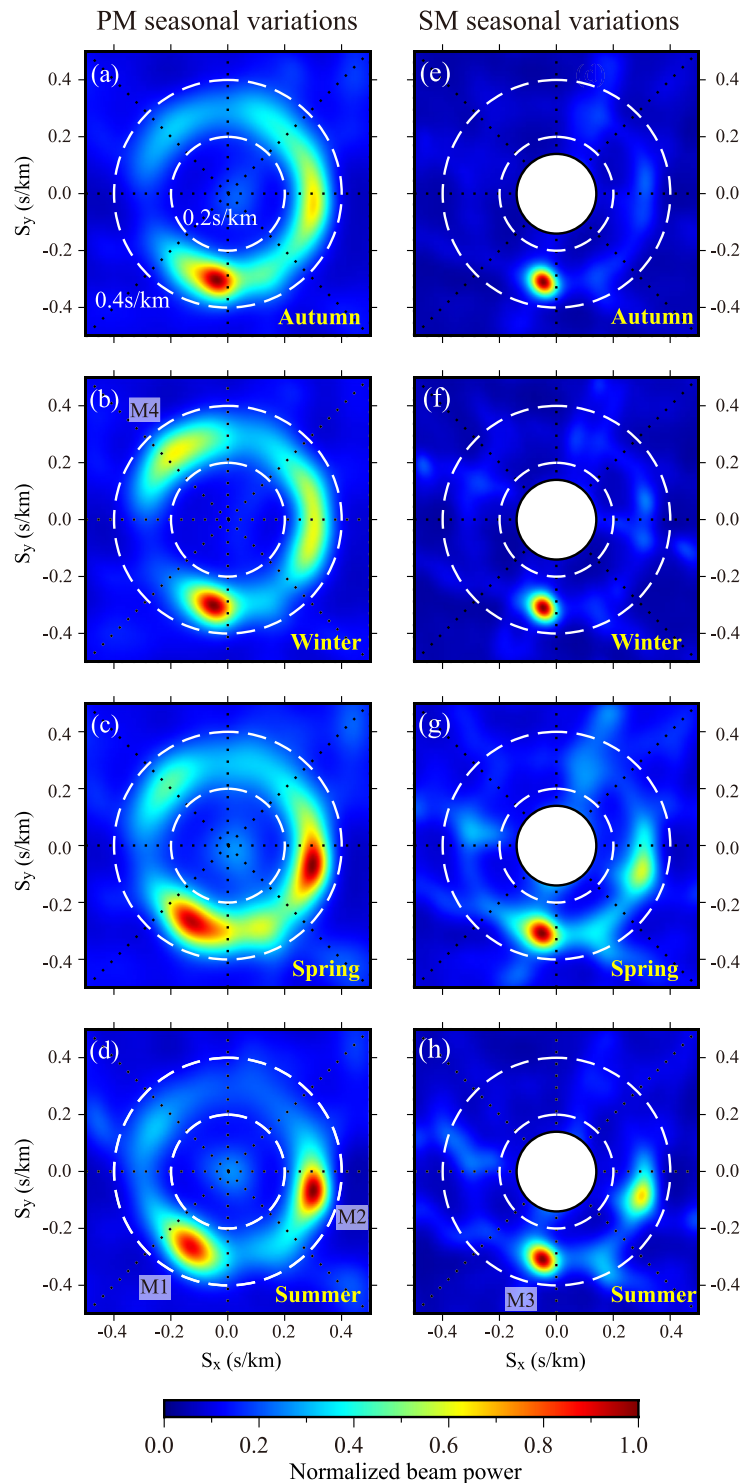


Figure 4. The seasonal variations of PM (45–95 mHz) and SM (95–155 mHz) recorded at TL array. The beamformer outputs are stacked seasonally using TL array data in autumn (September 2017–November 2017), winter (December 2017–February 2018), spring (March 2018–May 2018), and summer (June 2018). Each image is labeled with the season at right bottom corner. The strength and central azimuth of these arrivals appear to change with seasons. (a and b) The PM arrivals roughly come from three directions: $\sim 210^\circ$ (M1), $\sim 110^\circ$ (M2), and $\sim 320^\circ$ (M4). (e–h) The SM arrivals come from two azimuthal bands: $\sim 110^\circ$ (M2), $\sim 190^\circ$ (M3). At the frequency band of SM, we mute the body arrivals with an apparent velocity higher than 5 km/s, corresponding to a slowness less than 0.2 s/km.

across a broader azimuthal band. The NW arrival becomes much stronger in winter (M4 in Figure 4b), with a strength similar to the ~ESE signal.

In the SM frequency band, we observe a consistent major arrival with a slowness of ~ 0.3 s/km (~ 3.3 km/s) and an azimuth of $\sim 190^\circ$ in all the four beamforming images (M3 in Figures 4e–4h). The low apparent velocity suggests it is a surface wave arrival. During spring (Figure 4g) and summer (Figure 4h), there is a second arrival coming roughly from the ESE direction with a similar apparent velocity of ~ 3.3 km/s. In all the four beamforming images, we mute the body arrivals with an apparent velocity higher than 5 km/s, corresponding to a slowness less than 0.2 s/km. In general, body wave energy becomes stronger at the high frequency band of SM.

3.2. Azimuthal Distribution of Microseisms

To reveal more details of incoming microseisms, we repeat the beamforming analysis in 10 frequency bands centered from 50 to 140 mHz with a bandwidth of 10 mHz (Figures S1 and S2). We use data during one month in summer (June) and one month in winter (December) to ensure that all surface wave sources from northern and southern hemispheres are considered in this section.

In NH summer, the beamforming power of PM frequency band (45–95 mHz) shown in Figure 4d indicates two prominent directions of microseisms is in azimuth of $\sim 110^\circ$ and $\sim 210^\circ$, respectively, which are labeled as M2 and M1 in Figure 4d. Figure S1 suggests that M1 is dominant in the three low-frequency bands centered at 50, 60, and 70 mHz, while M2 is more prominent in the two high-frequency bands of 80 and 90 mHz. As for SM, the dominant source direction is $\sim 190^\circ$, labeled as M3 in Figure 4h. The arrival shows primarily in the three low-frequency bands centered at 100, 110, and 120 mHz (Figures S1f–S1h). In the three high-frequency bands of 120, 130, and 140 mHz, surface waves are much weaker than teleseismic body waves, which are focused at almost the center of the beamforming images (Figures S1h and S1i). It is consistent with previous beamforming results at 4–8 s and 8–12 s period bands using the ChinArray data (Wang et al., 2018). In Figure S1i, the body wave arrival has small slowness of ~ 0.03 s/km and a back azimuth of $\sim 180^\circ$.

In NH winter, the frequency content of the two primary arrivals, M1 and M2, appears to be reversed (Figures S2a–S2c). Here the SSW M1 arrival is dominant in the three high-frequency bands centered at 70, 80, and 90 mHz with a slight shift in azimuth from $\sim 210^\circ$ to $\sim 190^\circ$, suggesting that the geographic source region from SSW in summer and winter might be different. The same also occurred for the ESE M2 arrival. In winter, its low frequency content seems to be dominant, and the arriving azimuth shifts slightly toward the south. Both suggest that different source regions might be responsible for the M2 event in the summer and winter. For PM, a third arrival is observed from the NNW direction (labeled as M4 in Figure 4b). This signal is mostly seen in the two low-frequency bands of 50 and 60 mHz (Figures S2a and S2b). We also find a fifth signal in the azimuth band of $\sim 35^\circ$ – 60° , labeled as M5 in Figure S2b. It is relatively weak and mostly seen in the frequency range of 55–75 mHz. On the other hand, the SM beamforming spectra (Figures S2f–S2j) are more or less the same as those of the summer, with a dominant near south arrival of M3 except for the direction of teleseismic body waves focused at the center, which is directing to the northwest.

As shown in Figure 1, although the TL array is surrounded by the Bohai Bay to the northeast and the Yellow Sea to the southeast, the arrival directions of its recorded microseisms, however, do not seem to well match with the extending directions of local coastlines. We observe arrivals coming from the opposite directions of the local coastlines, such as the M1 (\sim SSW), M3 (near south), and M4 (NNW), are equally energetic as, if not stronger than those from the local coasts. This observation suggests that ocean waves at the Bohai Bay and the Yellow Sea barely contribute to Rayleigh wave signals in the PM and SM frequency bands recorded at the TL array. We speculate that the lack of excitation of microseisms is likely related to the bathymetry of the Bohai Bay and the Yellow Sea, which have an average depth of ~ 18 and ~ 44 m, respectively, making it difficult to develop large-amplitude ocean waves. Their sea floors are also flat with little slopes and reliefs, which are unfavorable for exciting microseisms (Arduin et al., 2015; Arduin, 2018).

The beamforming spectra of the two CI arrays in the PM and SM bands are shown in the top and bottom parts of Figure S3, respectively. We also employ the June and December records to show potential seasonal

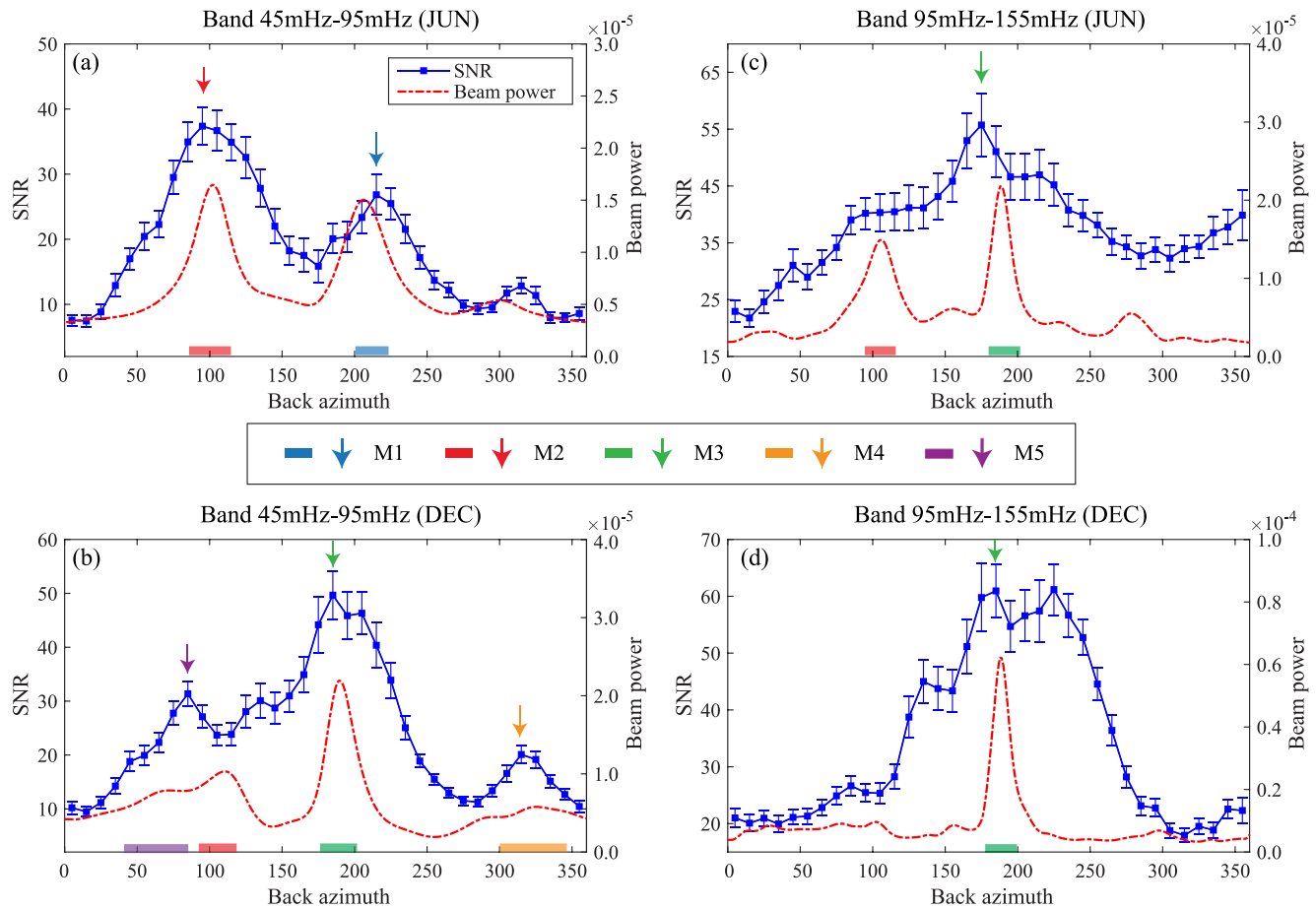


Figure 5. Azimuthal variation of beam power (red dot-dashed line) and the averaged SNR (blue line with squares) of the PM (left) and SM (right) NCFs computed from the June (top) and December (bottom) recordings. The uncertainty of SNR estimation is plotted by error bars. We marked five back azimuthal bands of high beam power by bars on the back azimuth axis. Arrows point to peaks of averaged SNR. (M1: blue; M2: red; M3: green; M4: yellow; M5: purple).

changes in noise sources recorded by the two arrays. The beamforming results from the two closely located arrays (left and right columns of Figure S3) are very similar, suggesting that our beamforming images are quite robust. In the NH summer, the PM (Figures S3a and S3b) and SM beamforming images (Figures S3e and S3f) are quite similar; but show a prominent arrival coming from an azimuth of $\sim 210^\circ$ with a slightly different slowness. In NH winter, the arrival direction of the strongest signal is NE in the PM band (Figures S3c and S3d), but changes to SSW in the SM band (Figures S3g and S3h). In addition, there is a weak arrival from the NW direction mostly seen in the PM band (Figures S3c and S3d). These directions are consistent with source regions suggested by high amplitude NCFs in the study of Tian and Ritzwoller (2015).

Next, we show results of the azimuthal variations of Rayleigh waves on NCFs computed from station pairs of the TL array in order to verify the above beamforming observations. We first bandpass filter all the monthly stacked NCFs in the frequency bands of 45–95 mHz and 95–155 mHz to obtain the PM and SM sets of NCFs. For each set of NCFs, we first compute their SNR_{cs} and then average them in 30° azimuthal bins using the method described in Section 2.2. Figure 5 shows the averaged SNR_{cs} of the PM (left) and SM (right) NCFs computed from the June (top) and December (bottom) recordings. For comparison, we also plot the beam power at PM and SM frequency bands in red dot-dashed lines. Here the beam power is $B(\omega, s, \varphi)$ defined in Equation 9, which is the beam power maximum of the surface wave slowness window (0.2–0.4 s/km) in the azimuthal direction φ .

In the PM frequency band, we observe two large peaks, one at $\sim 100^\circ$ (red arrow) and another at $\sim 215^\circ$ (blue arrow) in summer (Figure 5a), which correspond well to M2 and M1 arrivals in the beamforming image of

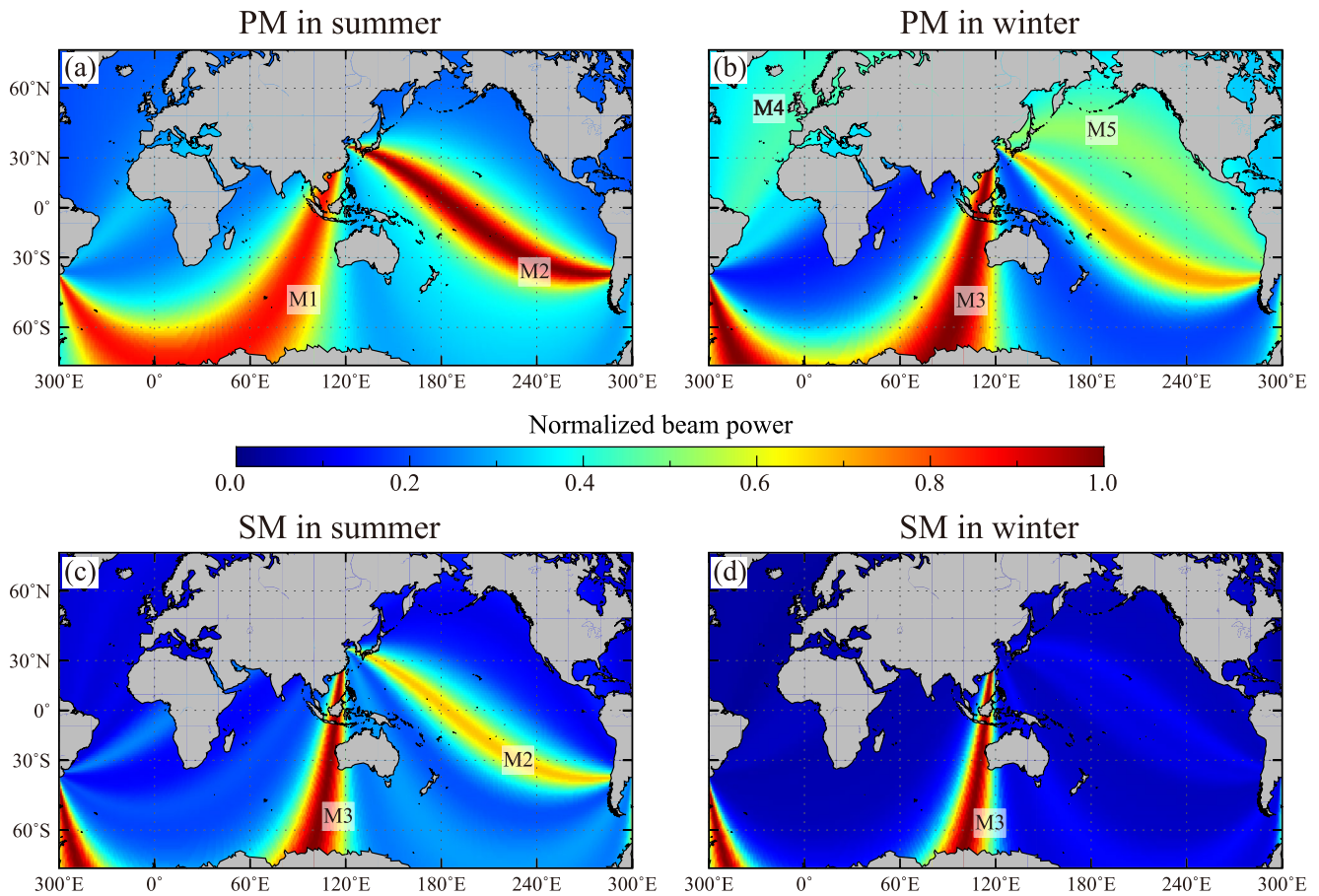


Figure 6. The back-projection of beam power along great circle paths extending from the TL array center for PM (top) and SM (bottom) computed from one-month recording in NH summer (June 2018) and NH winter (December 2017). Great circle paths are marked with their corresponding arrival number, M1–M5. The potential source regions of M1 (~210°) cover the northeast coast of the Indian Ocean, South Indian Ocean and the Southern Ocean. M2 (~110°) areas run across the southwest coast of Japan and the mid-to-south Pacific. The path of M3 (~190°) transects the South China sea, the Malay Archipelago, the west coast of Australia, and the Southern Ocean. M4 (~320°) path covers the coast of Europe, while M5 path transects coastal areas of northeast Japan, the Kuril Islands and Aleutian Islands.

Figure 4d. In winter (Figure 5b), the SNR_{cs} -azimuth curve shows three peaks, with the largest peak (green arrow) at ~190°. The second (purple arrow) and third (orange arrow) peaks are located at ~90° and ~320°, respectively. These peaks generally correlate with beamforming arrivals. In the SM frequency band, the SNR_{cs} tends to be high around the beam power peaks. However, the general correlation between the two curves is less significant. The SNR_{cs} peaks generally have larger azimuthal ranges than those of beamforming, suggesting they have lower resolutions in constraining microseismic source regions.

3.3. Source Regions of Rayleigh Wave Microseisms

Based on the results from beamforming and Rayleigh-wave SNR analyses, we obtain five azimuthal ranges of microseismic sources from the TL array. The back-projection of beam power along great circle paths extending from the TL array center is shown in Figure 6. We mark paths with their corresponding arrival number, M1–M5. High beam paths in NH summer cover three regions, M1 and M2 in the PM band (Figure 6a) and M2 and M3 in the SM band (Figure 6b). M1 in the azimuthal band of 200°–220° shows potential source regions including the northeast coast of the Indian Ocean, South Indian Ocean, and the Southern Ocean. Large storms generated in the Southern Ocean and the Indian Ocean impart the energy of M1 as they pass shallow water areas. The great circle path of M2 runs across the southwest coast of Japan and the mid-to-south Pacific. The path extends along the azimuth band of 180°–195° (M3) transects the South China Sea, the Malay Archipelago, and the west coast of Australia, and the Southern Ocean.

The great circle paths of the M4 and M5 arrivals observed primarily in the PM frequency band in the NH winter include large coastal regions of North Atlantic and North Pacific, respectively. M4 is probably generated at the coast of Europe, while M5 may be generated at coastal areas of northeast Japan, the Kuril Islands, and the Aleutian Islands. Both microseisms are likely related to large ocean waves from winter storms in North Pacific and North Atlantic. This is consistent with the excitation mechanism of a PM that attributes to forces by ocean swell at shallow depths on the shores (Hasselmann, 1963; Longuet-Higgins, 1950).

The back-projections of the beam powers of the CIN and CIS arrays in the SM frequency band in NH winter are shown in Figures 7a and 7b, respectively. Other beam back-projection maps of the two CI arrays are shown in Figure S4. While the back-projection images of the two arrays are very similar in the prominent source distribution, there are noticeable differences in the spread of weak energy bands. The combined image of the two closely located arrays (Figure 7c) cleans up local noise sources along the coast of California, while keeps the dominant beam extending from the two arrays along $\sim 210^\circ$ (Figure 7c). The combined SM beam projection of NH summer is shown in Figure 7d, and those of PM in the winter and summer are shown in Figures 7e and 7f, respectively. These combined back-projections suggest potential source regions for the two high amplitude arrivals, which include the North Atlantic, mid-to-south Pacific, the Southern Ocean, and South Indian Oceans. The weak arrival from the NW direction shown in the PM frequency band in the NH winter seems to be related to the north and west Pacific regions.

The combined beam-power back-projection images are shown in Figure 8. High energy clusters arise at the intersection of individual beams shown in Figures 6 and 7, which we attribute as the Rayleigh wave source regions. In the NH summer, we identify two source regions for generating PM, one around the Polynesia islands in the southern Pacific Ocean and another one around the Kerguelen Islands in the southern Indian Ocean (Figure 8a). The Polynesia islands also appear to be one source region for the SM. Another SM source is located along the Southern Ocean coast at $\sim 100^\circ\text{E}$ (Figure 8b). In the NH winter, the South China Sea and the NE Atlantic Ocean are the two dominant source regions for the PM (Figure 8c) observed in eastern China and southern California. There is a third source region in the NW Pacific Ocean that produces a much weak arrival at the TL and CI arrays. The main SM source lies at the same spot in the Southern Ocean at $\sim 100^\circ\text{E}$ (Figure 8d).

In summary, we locate five source regions that produce the microseisms recorded by the TL and CI arrays (Figure 9a). Since they correspond to the five Rayleigh wave arrivals, M1–M5, observed at the TL array, here we also use the same label to mark the five source regions. Microseism sources excited in NH summer and winter are indicated by solid and dashed ellipses, respectively. The dotted ellipse shows source regions that are active all year round.

4. Discussion

It is widely believed that microseisms are generated by the coupling between ocean waves and solid earth. In Figures 9b and 9c, we show the monthly averaged ocean wave height during December 2017 and June 2018. The data was downloaded from the global monthly mean ocean wave parameter dataset based on the FIO Earth System Model (Bao et al., 2020; Song, Bao, Zhang, et al., 2020).

Several previous studies (e.g., Liu et al., 2016; Wang et al., 2018) have identified the Kerguelen Islands in the South Indian Ocean (M1, blue ellipse in Figure 9a) as a source region of teleseismic body waves in microseisms observed in China. Our analyses suggest that it is also an area that produces strong Rayleigh waves in primary microseisms recorded in eastern China and southern California. This suggests that Rayleigh-wave and body-wave microseisms can share source locations. Traer et al. (2012) analyzed noises recorded by the USArray and found that a prominent source azimuth of $\sim 210^\circ$ of the microseisms in NH summer, which is consistent with our observation at the CI arrays. They further correlated the noise data with ocean wave activity and attributed Polynesian islands to be the likely source region for the PM of the USArray. Our back-projection analyses clearly indicate that it is also a source region of the PM (M2, red ellipse in Figure 9a) observed by the TL array during the NH summer. Figure 8a shows that the Kerguelen Islands and the Polynesia islands are the two main source regions for the PM in the NH summer. They are likely originated from large storms in the Southern Ocean and the South Pacific respectively when ocean

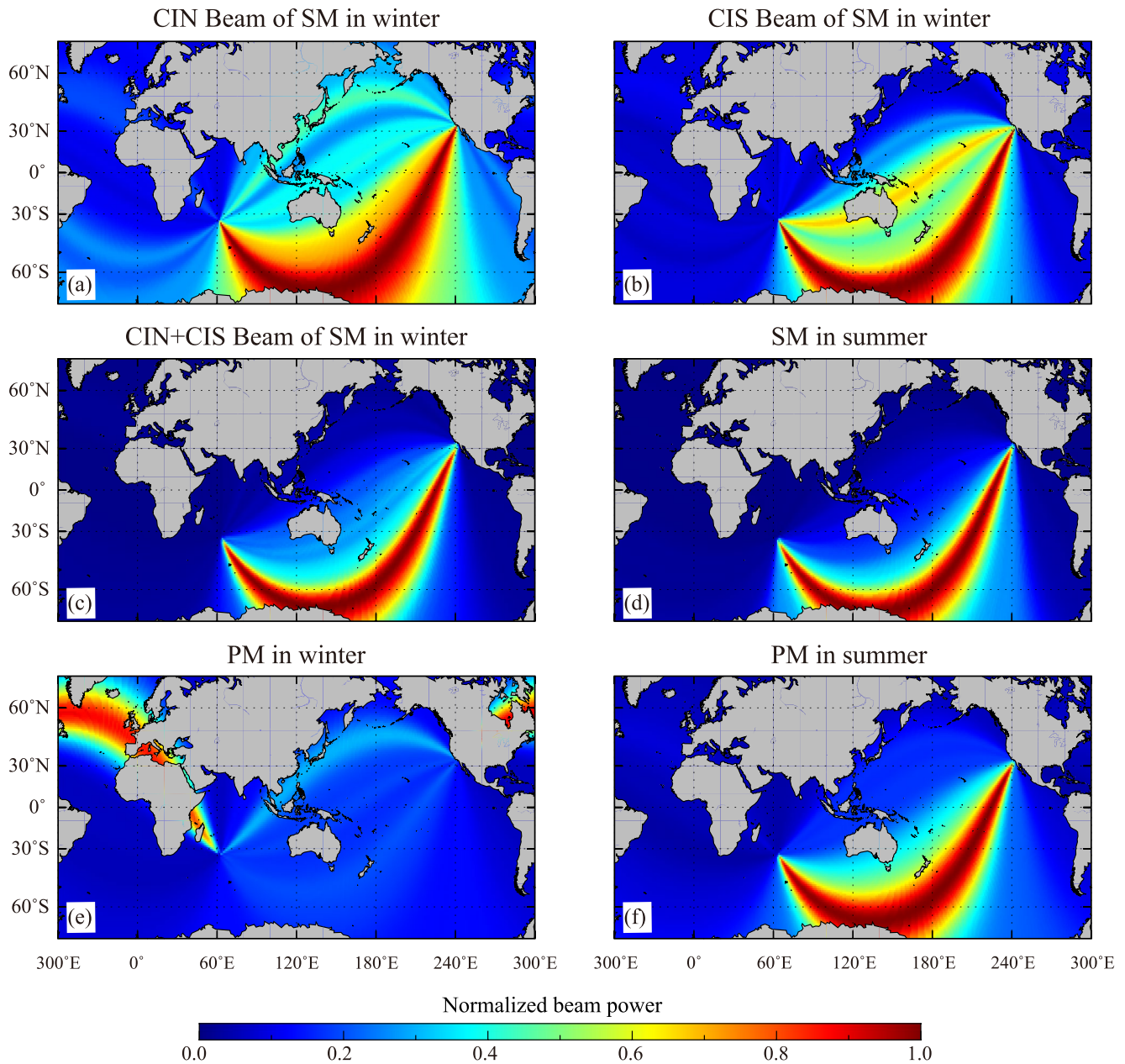


Figure 7. The back-projections of the beam powers from CIN and CIS arrays in NH winter (December 2017) and NH summer (June 2018). (a and b) At the SM frequency band in NH winter, beam power is normalized and back-projected along the great circle path using data of CIN array panel (a) and CIS array panel (b). (c) The combined image of panels (a) and (b) for SM in NH winter. The combined image of the two neighboring arrays cleans up local noise sources along the coast, while keeps the distant and persistent arrival path extending along the azimuth of $\sim 210^\circ$. (d)–(f) The combined back-projections of the beam powers for SM in summer panel (d), PM in winter panel (e), PM in summer panel (f).

waves pass the two island chains (Figure 9b). This suggests that Rayleigh wave PM can be excited not only in continental coastal regions but also in areas close to islands in open seas.

Three source areas are identified for the PM in NH winter (Figure 9a), which are the western coast of Europe (M4, yellow dashed ellipse), coastal areas of NW Pacific (M5, purple dashed ellipse), and the South China Sea (M3, green dashed ellipse). The M4 area coincides with the region with the maximum ocean wave height in the North Atlantic in NH winter (Figure 9c). It covers the source region of Rayleigh waves microseisms identified by Retaillieu et al. (2017) using data recorded by an array in North America and a station in west Europe. However, the predicted source region in our study is much broader and the peak is

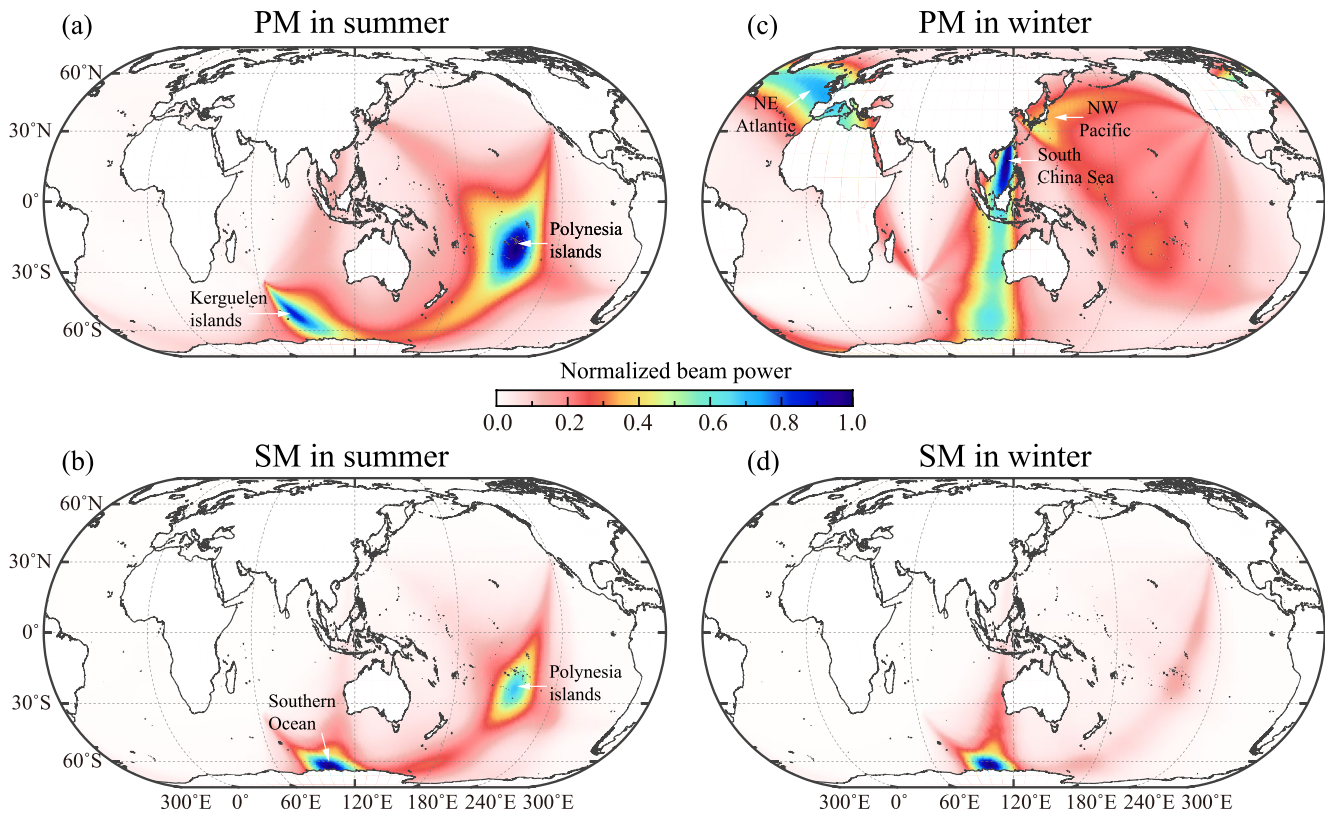


Figure 8. Final beam power back-projection images combined from TL, CIN and CIS arrays. (a) PM in summer. (b) PM in winter. (c) SM in summer. (d) SM in winter. Each high beam power area is pointed by a white arrow with the location name beside it. In NH summer, located source regions include Polynesia Islands, Kerguelen Islands, the Southern Ocean. In NH winter, sources cover the NW Pacific Ocean, the NE Atlantic, South China Sea, and the Southern Ocean.

slightly shifted southward (Figure 8b). The resolution is limited because the M4 area is close to midpoints of great circle paths where have the largest width. The M5 source region includes the Pacific coast of northeast Japan, the Kuril Islands, and the Aleutian Islands, which has been identified as one of the source areas for body wave in microseisms recorded in China (Liu et al., 2016), but has never been reported as a dominant Rayleigh wave PM source in NH winter. For the third source region in the South China Sea (M3), the high power is contributed from the intersection between the $\sim 190^\circ$ path from the TL array and the NW paths from CI arrays. However, it is well accepted that the NW signal recorded in the US is generated at coastal areas of the North Pacific. In addition, along the great circle path of M3, there are other beam power peaks together with large wave height, such as the western coast of Australia, and the Southern Ocean (Figures 8c and 9c). Therefore, the $\sim 190^\circ$ arrival (M3) may be from farther areas rather than the South China Sea. The ambiguity of M3 source location may be avoided by results from more arrays in China.

Two key aspects of PM generation are ocean activities and topographic features. Besides wave heights, PM excitation is controlled by the features of shoreline and bathymetry, for example, a sloping sea bottom (Ardhuin et al., 2015; Hasselmann, 1963) or small-scale topographic features (Ardhuin, 2018). The PM amplitude can be much larger over a wavy bottom with similar wavelengths of ocean waves (Ardhuin, 2018). This may be the reason why some coastal areas with medium ocean wave heights can generate strong PM signals, like the Polynesian islands, the Kuril Islands, and coastal areas of northeast Japan.

At the SM frequency band, few previous studies are focusing on the Rayleigh wave component. Here we identify two dominant source locations at Polynesian islands (M2, red ellipse in Figure 9a) and the Southern Ocean (M3, green dotted ellipse). The beam power peak at the M3 area matches well with the averaged ocean wave height peak, while the M2 area at the Polynesian islands shows medium ocean wave height (Figures 9b and 9c). In addition, we noticed another small-amplitude peak between New Zealand and Antarctica in the combined beam images in the SM band (Figure 8b), which is much weaker than the five

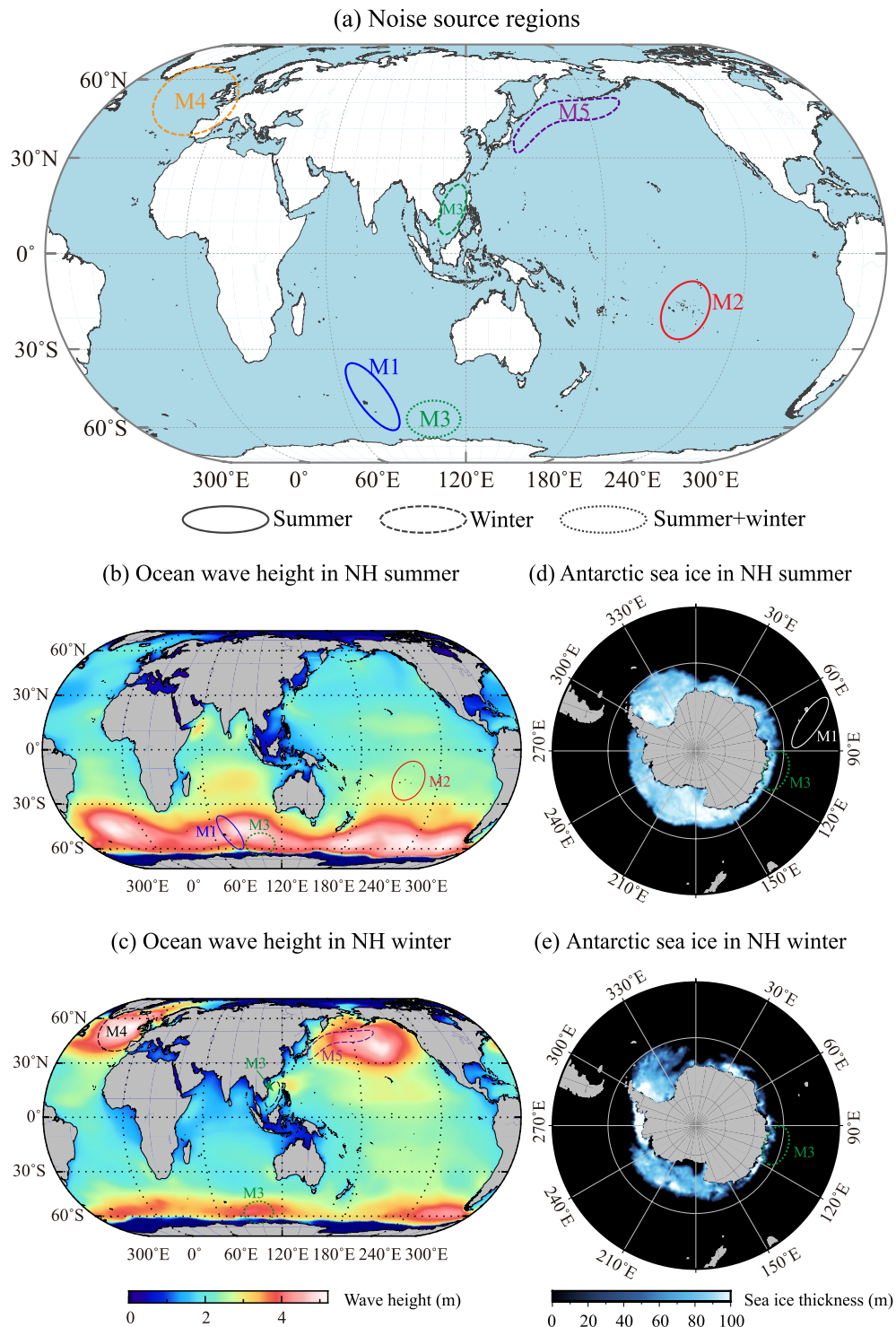


Figure 9. (a) Source regions of Rayleigh-wave microseisms located by multi-array beam power back-projection. M1: Kerguelen Islands in the southern Indian Ocean (blue solid ellipse). M2: Polynesia islands in the South Pacific (red solid ellipse). M3: the South China Sea (green dashed ellipse) and the Southern Ocean (green dotted ellipse). M4: the North Atlantic (yellow dashed ellipse). M5: coastal areas of northeast Japan, the Kuril Islands and Aleutian Islands (purple dashed ellipse). Microseism sources excited in NH summer and winter are indicated by solid and dashed ellipses, respectively. The dotted ellipse shows source regions that are active all year round. (b) Monthly averaged global significant ocean wave heights in NH summer (June 2018). (c) The same as panel (b) but in NH winter (December 2017). The estimated source regions are marked by ellipses. (d) Sea ice distribution around the Antarctic in NH summer (June 15, 2018). (e) The same as panel (d) but in NH winter (December 15, 2017). M1 and M3 are indicated by solid and dotted ellipses, respectively.

identified events such that we did not number it as a dominant and persistent source in Section 3. This area appears to have high amplitude ocean waves in the NH summer (Figure 9b). The theoretical explanation of SM generation is due to the interaction between waves with similar periods and opposing propagation. Opposing wave patterns arise through opposing winds, multiple storm systems, or coastal reflections from an obstacle like shoreline and iceberg (Ardhuin et al., 2011; Hillers et al., 2012). M2 area is located close to strong ocean storms in South Pacific especially in NH summer (Figure 9c). Ocean wave reflections at the shoreline of Polynesian islands can produce opposing wave interactions and generate SM. In Figures 9d and 9e, we indicate source locations in sea ice concentration maps at the Antarctic area on June 15, 2018 and December 15, 2017. The maps are derived from the Near Real-Time SSM/I EASE-Grid Daily Global Ice Concentration and Snow Extent product (Near real-time Ice and Snow Extent, NISE), which was created by the National Snow and Ice Data Center (NSIDC) in Boulder, Colorado (Brodzik & Stewart, 2016). We did not notice any special of the M3 area, which is indicated by the green dotted ellipse, in terms of sea ice shape and thickness, as well as changes between winter and summer. Therefore, it is unclear to us why the Antarctic coast at M3 is so efficient to generate counter-propagating ocean waves.

It should be noted that our data set covers a duration of 10 months from September 2017 to June 2018, hence it reflects microseism distribution and ocean activities of a particular time window. We notice that strong SM signals recorded by the TL array and CI arrays come only from the southern hemisphere (Figures 6c, 6d, 7c and 7d). In other words, there are no significant SM sources in the northern hemisphere during the 10-month period. Also, the observed source distribution of SM shows little seasonal variations. Our observations on SM distribution are consistent with the results of Stehly et al. (2006), which are derived from a sparse array in southern California. However, Traer et al. (2012) showed that there are significant SM signals originated from the North Pacific and North Atlantic during the NH winter time. Such strong SM signals are also expected from numerical modeling of microseisms (Stutzmann et al., 2012). To investigate possible causes of this discrepancy, we first examined whether it can be caused by different ways in data preprocessing as we notice that Traer et al. (2012) employed a different temporal normalization method from ours. We applied three temporal normalization methods to the continuous records: (a) clipping data using one standard deviation as the threshold (Gerstoft & Tanimoto, 2007), (b) clipping data using a low threshold proposed by Traer et al. (2012), and (c) no time-domain normalization. The beamforming results of the three arrays are shown in Figure S5. The beamforming images from different preprocessing at each array are almost identical. The dominant SM direction remains unchanged, while the weaker signals show very small variations in beamforming amplitude. This demonstrates that the lack of SM signals from the North Pacific and North Atlantic in our data is unlikely an artifact of data preprocessing.

One possible cause is that the array used by Traer et al. (2012) has an aperture of $\sim 2,000$ km, almost 20 times larger than our arrays, so it is more efficient in focusing weak signals. We notice that the direction of the strongest SM detected by Traer et al. (2012) is similar to ours, while those coming from North Pacific and North Atlantic are much weaker. Therefore, it is possible that these weaker SMs are not sufficiently enhanced enough to appear on our beamforming images.

On the ocean wave height maps, two more areas in SH show strong ocean activities but are not identified in our source distribution map. One is the open sea area between South America and the Antarctic. The area was observed as a Rayleigh wave source by USArray data (Traer et al., 2012). The other is the high wave region of the Southern Ocean between Africa and the Antarctic. Strong *P*-wave SM was observed to originate from the area by arrays in Africa (Euler et al., 2014). Theoretically, both may generate strong Rayleigh-wave SM because of the interaction between local large-amplitude waves and reflected waves from coasts. In our results of California arrays, we indeed observe weak signals from SSE in beamforming results of the CIN array. However, it is absent in the beam images of the CIS array, which makes the two areas thoroughly excluded from combined results. In addition, both sources are unobservable at TL array in China. They were not located by Wang et al. (2018) using ChinArray as well. The arrivals may be blocked by closer and stronger signals like M2 and M3. In general, if a microseism source is located far away from one of the arrays, then it would not appear in the combined beamforming image. In other words, it is likely some microseism sources could be suppressed if they are below the detectability of one of the arrays. This might explain why some microseism sources reported by previous studies are missing in our combined images. The inclusion

of more stations and other arrays together with an improved algorithm in integrating individual beam powers is expected to obtain a more comprehensive global distribution of PM and SM sources.

5. Conclusions

We use the beamforming method and Rayleigh wave amplitude-azimuth variation analyses to investigate the distribution of Rayleigh-wave microseisms. Seasonal variations are clearly observable for PM but are less prominent for SM. The mismatch between local coastlines and the azimuthal distribution of microseisms suggests that local ocean activities have little contribution to microseisms recorded by the TL array. The back-projections of beam power show potential source regions transecting large swaths of ocean. By combining the TL array and two additional arrays in southern California, we locate five strong and persistent microseisms at a global scale. At PM frequency band, microseisms are mainly located at Kerguelen Islands (M1), Polynesia islands (M2), western coast of Europe (M4), and coastal regions of the North Pacific (M5). There are several plausible source locations for M3 including the South China Sea and farther areas such as the western coast of Australia and the Southern Ocean. The generation of PM is interpreted as ocean waves impacting shallow water areas, such as continental coastal regions and the shore of islands in open sea areas. Based on our observation from the three arrays, we identify two SM source locations including Polynesia islands (M2) and the Southern Ocean coast at $\sim 100^\circ\text{E}$ (M3). Wave reflections on shorelines provide the opposing waves with a similar period to generate strong SM.

Data Availability Statement

Seismic data of CI network can be accessed from the Incorporated Research Institutions for Seismology (IRIS) Data Management Center (DMC) (<https://doi.org/10.7914/SN/CI>). TL array support data of this study are available at <http://dx.doi.org/10.17632/c9zrmy7n9r.1> website. The ocean wave height data are available at <https://doi.org/10.6084/m9.figshare.c.4819503.v1> website (Song, Bao, Shu, et al., 2020). The sea ice distribution maps were derived from the Near Real-Time SSM/I EASE-Grid Daily Global Ice Concentration and Snow Extent product (Near real-time Ice and Snow Extent, NISE, https://neo.sci.gsfc.nasa.gov/view.php?datasetId=NISE_D).

References

- Ardhuin, F. (2018). Large-scale forces under surface gravity waves at a wavy bottom: A mechanism for the generation of primary microseisms. *Geophysical Research Letters*, 45(16), 8173–8181. <https://doi.org/10.1029/2018gl078855>
- Ardhuin, F., Gualtieri, L., & Stutzmann, E. (2015). How ocean waves rock the Earth: Two mechanisms explain microseisms with periods 3 to 300 s. *Geophysical Research Letters*, 42(3), 765–772. <https://doi.org/10.1002/2014gl062782>
- Ardhuin, F., Stutzmann, E., Schimmel, M., & Mangeney, A. (2011). Ocean wave sources of seismic noise. *Journal of Geophysical Research*, 116(C9), C09004. <https://doi.org/10.1029/2011JC006952>
- Bao, Y., Song, Z., & Qiao, F. (2020). FIO-ESM version 2.0: Model description and evaluation. *Journal of Geophysical Research: Oceans*, 125(6), e2019JC016036. <https://doi.org/10.1029/2019jc016036>
- Bensen, G. D., Ritzwoller, M. H., Barmin, M. P., Levshin, A. L., Lin, F., Moschetti, M. P., et al. (2007). Processing seismic ambient noise data to obtain reliable broad-band surface wave dispersion measurements. *Geophysical Journal International*, 169(3), 1239–1260. <https://doi.org/10.1111/j.1365-246x.2007.03374.x>
- Biggs, D. S. C., & Andrews, M. (1997). Acceleration of iterative image restoration algorithms. *Applied Optics*, 36(8), 1766–1775. <https://doi.org/10.1364/ao.36.001766>
- Brodzik, M. J., & Stewart, J. S. (2016). Near-real-time SSM/I-SSMIS EASE-grid daily global ice concentration and snow extent, Version 5. NASA National Snow and Ice Data Center Distributed Active Archive Center. <https://doi.org/10.5067/3KB2JPLFPK3R>
- Bromirski, P. D., & Duennebieber, F. K. (2002). The near-coastal microseism spectrum: Spatial and temporal wave climate relationships. *Journal of Geophysical Research*, 107(B8), ESE5-1–ESE5-20. <https://doi.org/10.1029/2001jb000265>
- Bromirski, P. D., Duennebieber, F. K., & Stephen, R. A. (2005). Mid-ocean microseisms. *Geochemistry, Geophysics, Geosystems*, 6(4), Q04009. <https://doi.org/10.1029/2004GC000768>
- Cessaro, R. K. (1994). Sources of primary and secondary microseisms. *Bulletin of the Seismological Society of America*, 84(1), 142–148.
- Euler, G. G., Wiens, D. A., & Nyblade, A. A. (2014). Evidence for bathymetric control on the distribution of body wave microseism sources from temporary seismic arrays in Africa. *Geophysical Journal International*, 197(3), 1869–1883. <https://doi.org/10.1093/gji/ggu105>
- Gal, M., Reading, A. M., Rawlinson, N., & Schulte-Pelkum, V. (2018). Matched field processing of three-component seismic array data applied to Rayleigh and Love microseisms. *Journal of Geophysical Research: Solid Earth*, 123(8), 6871–6889. <https://doi.org/10.1029/2018JB015526>
- Gerstoft, P., Fehler, M. C., & Sabra, K. G. (2006). When Katrina hit California. *Geophysical Research Letters*, 33(17), L17308. <https://doi.org/10.1029/2006GL027270>

Acknowledgments

The authors thank all the people involved in the TL array project for providing the continuous data of the TL array, the Southern California Earthquake Data Center (SCEDC) for providing the seismic data of the CI network, and the National Snow and Ice Data Center (NSIDC) for providing sea ice distribution data. The authors are grateful to all members of the Seismology and Tectonics at Rice University for comments and discussion. The authors also thank two anonymous reviewers for their constructive and thoughtful comments and suggestions, which have significantly improved the quality of this study. This study was jointly supported by the National Natural Science Foundation of China (41630209, 41821002, 41922028, 41874149), National Key Research and Development Program of China (2019YFC0605503), the Strategic Priority Research Program of the Chinese Academy of Sciences (XDA14010303), the Major Scientific and Technological Projects of CNPC (ZD2019-183-003), and the China Scholarship Council (201906450056).

- Gerstoft, P., Shearer, P. M., Harmon, N., & Zhang, J. (2008). Global P, PP, and PKP wave microseisms observed from distant storms. *Geophysical Research Letters*, *35*(23), L23306. <https://doi.org/10.1029/2008GL036111>
- Gerstoft, P., & Tanimoto, T. (2007). A year of microseisms in southern California. *Geophysical Research Letters*, *34*(20), L20304. <https://doi.org/10.1029/2007GL031091>
- Hasselmann, K. (1963). A statistical analysis of the generation of microseisms. *Reviews of Geophysics*, *1*(2), 177–210. <https://doi.org/10.1029/RG001i002p00177>
- Hillers, G., Graham, N., Campillo, M., Kedar, S., Landès, M., & Shapiro, N. (2012). Global oceanic microseism sources as seen by seismic arrays and predicted by wave action models. *Geochemistry, Geophysics, Geosystems*, *13*(1), Q01021. <https://doi.org/10.1029/2011gc003875>
- Ishii, M., Shearer, P. M., Houston, H., & Vidale, J. E. (2007). Teleseismic P wave imaging of the 26 December 2004 Sumatra-Andaman and 28 March 2005 Sumatra earthquake ruptures using the Hi-net array. *Journal of Geophysical Research*, *112*(B11), B11307. <https://doi.org/10.1029/2006JB004700>
- Juretzek, C., & Hadziioannou, C. (2016). Where do ocean microseisms come from? A study of Love-to-Rayleigh wave ratios. *Journal of Geophysical Research: Solid Earth*, *121*(9), 6741–6756. <https://doi.org/10.1002/2016JB013017>
- Juretzek, C., & Hadziioannou, C. (2017). Linking source region and ocean wave parameters with the observed primary microseismic noise. *Geophysical Journal International*, *211*(3), 1640–1654. <https://doi.org/10.1093/gji/ggx388>
- Kedar, S., Longuet-Higgins, M., Webb, F., Graham, N., Clayton, R., & Jones, C. (2008). The origin of deep ocean microseisms in the North Atlantic Ocean. *Proceedings of the Royal Society A: Mathematical, Physical & Engineering Sciences*, *464*, 777–793. <https://doi.org/10.1098/rspa.2007.0277>
- Landès, M., Hubans, F., Shapiro, N. M., Paul, A., & Campillo, M. (2010). Origin of deep ocean microseisms by using teleseismic body waves. *Journal of Geophysical Research*, *115*(B5), B05302. <https://doi.org/10.1029/2009JB006918>
- Liu, Q., Koper, K. D., Burlacu, R., Ni, S., Wang, F., Zou, C., et al. (2016). Source locations of teleseismic P, SV, and SH waves observed in microseisms recorded by a large aperture seismic array in China. *Earth and Planetary Science Letters*, *449*, 39–47. <https://doi.org/10.1016/j.epsl.2016.05.035>
- Liu, Q., Ni, S., Qiu, Y., Zeng, X., Zhang, B., Wang, F., et al. (2020). Observation of teleseismic S wave microseisms generated by typhoons in the western Pacific Ocean. *Geophysical Research Letters*, *47*(19), e2020GL089031. <https://doi.org/10.1029/2020gl089031>
- Longuet-Higgins, M. S. (1950). A theory of the origin of microseisms. *Philosophical Transactions of the Royal Society of London. Series A, Mathematical and Physical Sciences*, *243*(857), 1–35. <https://doi.org/10.1098/rsta.1950.0012>
- Moschetti, M. P., Ritzwoller, M. H., & Shapiro, N. M. (2007). Surface wave tomography of the western United States from ambient seismic noise: Rayleigh wave group velocity maps. *Geochemistry, Geophysics, Geosystems*, *8*(8), Q08010. <https://doi.org/10.1029/2007GC001655>
- Nishida, K. (2017). Ambient seismic wave field. *Proceedings of the Japan Academy, Series B*, *93*(7), 423–448. <https://doi.org/10.2183/pjab.93.026>
- Nishida, K., Kawakatsu, H., Fukao, Y., & Obara, K. (2008). Background Love and Rayleigh waves simultaneously generated at the Pacific Ocean floors. *Geophysical Research Letters*, *35*(16), L16307. <https://doi.org/10.1029/2008GL034753>
- Nishida, K., & Takagi, R. (2016). Teleseismic S wave microseisms. *Science*, *353*(6302), 919–921. <https://doi.org/10.1126/science.aaf7573>
- Park, S., & Hong, T. K. (2020). Typhoon-induced microseisms around the South China Sea. *Seismological Society of America*, *91*(6), 3454–3468. <https://doi.org/10.1785/0220190310>
- Pyle, M. L., Koper, K. D., Euler, G. G., & Burlacu, R. (2015). Location of high-frequency P wave microseismic noise in the Pacific Ocean using multiple small aperture arrays. *Geophysical Research Letters*, *42*(8), 2700–2708. <https://doi.org/10.1002/2015GL063530>
- Retailleau, L., Boué, P., Stehly, L., & Campillo, M. (2017). Locating microseism sources using spurious arrivals in intercontinental noise correlations. *Journal of Geophysical Research: Solid Earth*, *122*(10), 8107–8120. <https://doi.org/10.1002/2017JB014593>
- Retailleau, L., & Gualtieri, L. (2019). Toward high-resolution period-dependent seismic monitoring of tropical cyclones. *Geophysical Research Letters*, *46*(3), 1329–1337. <https://doi.org/10.1029/2018GL080785>
- Richardson, W. H. (1972). Bayesian-based iterative method of image restoration. *Journal of the Optical Society of America*, *62*(1), 55–59. <https://doi.org/10.1364/josa.62.000055>
- Rost, S., & Thomas, C. (2002). Array seismology: Methods and applications. *Reviews of Geophysics*, *40*(3), 2-1–2-27. <https://doi.org/10.1029/2000rg000100>
- SCEDC. (2013). *Southern California Earthquake Center*. Caltech. Dataset. <https://doi.org/10.7909/C3WD3xH1>
- Shapiro, N. M., Campillo, M., Stehly, L., & Ritzwoller, M. H. (2005). High-resolution surface-wave tomography from ambient seismic noise. *Science*, *307*(5715), 1615–1618. <https://doi.org/10.1126/science.1108339>
- Song, Z., Bao, Y., Shu, Q., Song, Y., Yang, X., & Qiao, F. (2020). Simulated long-term monthly ocean surface waves parameters from FIO-ESM v2.0 CMIP6 experiments for past, present, and future climate research (Version 1). Figshare. <https://doi.org/10.6084/m9.figshare.c.4819503.v1>
- Song, Z., Bao, Y., Zhang, D., Shu, Q., Song, Y., & Qiao, F. (2020). Centuries of monthly and 3-hourly global ocean wave data for past, present, and future climate research. *Scientific Data*, *7*(1), 1–11. <https://doi.org/10.1038/s41597-020-0566-8>
- Stehly, L., Campillo, M., & Shapiro, N. M. (2006). A study of the seismic noise from its long-range correlation properties. *Journal of Geophysical Research*, *111*(B10), B10306. <https://doi.org/10.1029/2005jb004237>
- Stutzmann, E., Arduhuin, F., Schimmel, M., Mangeney, A., & Patau, G. (2012). Modelling long-term seismic noise in various environments. *Geophysical Journal International*, *191*(2), 707–722. <https://doi.org/10.1111/j.1365-246x.2012.05638.x>
- Tian, Y., & Ritzwoller, M. H. (2015). Directionality of ambient noise on the Juan de Fuca plate: Implications for source locations of the primary and secondary microseisms. *Geophysical Journal International*, *201*(1), 429–443. <https://doi.org/10.1093/gji/ggv024>
- Traer, J., Gerstoft, P., Bromirski, P. D., & Shearer, P. M. (2012). Microseisms and hum from ocean surface gravity waves. *Journal of Geophysical Research*, *117*(B11), B11307. <https://doi.org/10.1029/2012JB009550>
- Wang, W., Gerstoft, P., & Wang, B. (2018). Seasonality of P wave microseisms from NCF-based beamforming using ChinArray. *Geophysical Journal International*, *213*(3), 1832–1848. <https://doi.org/10.1093/gji/gyy081>
- Ward Neale, J., Harmon, N., & Srokosz, M. (2018). Improving microseismic P wave source location with multiple seismic arrays. *Journal of Geophysical Research: Solid Earth*, *123*(1), 476–492. <https://doi.org/10.1002/2017JB015015>
- Xiao, H., Xue, M., Pan, M., & Gao, J. (2018). Characteristics of microseisms in South China. *Bulletin of the Seismological Society of America*, *108*(5A), 2713–2723. <https://doi.org/10.1785/0120170237>
- Xiao, H., Xue, M., Yang, T., Liu, C., Hua, Q., Xia, S., et al. (2018). The characteristics of microseisms in South China Sea: Results from a combined data set of OBSs, broadband land seismic stations, and a global wave height model. *Journal of Geophysical Research: Solid Earth*, *123*(5), 3923–3942. <https://doi.org/10.1029/2017JB015291>

- Xu, Y., Koper, K. D., Sufri, O., Zhu, L., & Hutko, A. R. (2009). Rupture imaging of the Mw 7.9 12 May 2008 Wenchuan earthquake from back projection of teleseismic P waves. *Geochemistry, Geophysics, Geosystems*, *10*(4), Q04006. <https://doi.org/10.1029/2008gc002335>
- Yang, Y., & Ritzwoller, M. H. (2008). Characteristics of ambient seismic noise as a source for surface wave tomography. *Geochemistry, Geophysics, Geosystems*, *9*(2), Q02008. <https://doi.org/10.1029/2007GC001814>
- Yang, Y., Ritzwoller, M. H., Levshin, A. L., & Shapiro, N. M. (2007). Ambient noise Rayleigh wave tomography across Europe. *Geophysical Journal International*, *168*(1), 259–274. <https://doi.org/10.1111/j.1365-246X.2006.03203.x>
- Yang, Y., Zheng, Y., Chen, J., Zhou, S., Ceylan, S., Sandvol, E., et al. (2010). Rayleigh wave phase velocity maps of Tibet and the surrounding regions from ambient seismic noise tomography. *Geochemistry, Geophysics, Geosystems*, *11*(8), Q08010. <https://doi.org/10.1029/2010GC003119>
- Ying, Y., Bean, C. J., & Bromirski, P. D. (2014). Propagation of microseisms from the deep ocean to land. *Geophysical Research Letters*, *41*(18), 6374–6379. <https://doi.org/10.1002/2014GL060979>
- Zeng, X., & Ni, S. (2010). A persistent localized microseismic source near the Kyushu Island, Japan. *Geophysical Research Letters*, *37*(24), L24307. <https://doi.org/10.1029/2010GL045774>
- Zeng, X., & Ni, S. (2014). Evidence for an independent 26-s microseismic source near the Vanuatu Islands. *Pure and Applied Geophysics*, *171*(9), 2155–2163. <https://doi.org/10.1007/s00024-014-0811-1>
- Zhang, J., Gerstoft, P., & Bromirski, P. D. (2010). Pelagic and coastal sources of P-wave microseisms: Generation under tropical cyclones. *Geophysical Research Letters*, *37*(15), L15301. <https://doi.org/10.1029/2010GL044288>